

# An Analysis of a Particle Size Frequency Distribution of a 6.4-gram Aggregate Sample of Asteroid (101955) Bennu

Savannah Smith<sup>1</sup>, Andrew J. Ryan<sup>1</sup>, and Zack Gainsforth<sup>2</sup>

<sup>1</sup>Lunar and Planetary Laboratory, University of Arizona, Tucson, USA.

<sup>2</sup>Department of Space Sciences, University of California Berkeley, Berkeley, USA.

## Abstract

The OSIRIS-REx mission returned a sample of near-Earth asteroid (101955) Bennu to improve our understanding of our solar system's formation and evolution. This paper examines a 6.4-gram aggregate sample (OREX-800107-0) consisting of smaller particles from Bennu's surface, ranging from less than 17 microns—referred to as unresolved material—to approximately 7 millimeters. The particles were segmented by training a machine learning algorithm that relied on user annotations for voxel classification, and the longest axis of these particles was determined in two different ways for each image processing software—first being a bounding box algorithm approximation and second being the maximum Feret diameter. These longest axes were counted in a cumulative frequency per volume plot in order to produce a normalized, cumulative particle size frequency distribution (PSFD) plot. Other researchers have determined a power-law slope of approximately  $-2.1 \pm 0.1$  for a particle size range of 1.1 mm to 36.6 mm, noting that as the particle size decreases, it becomes more difficult to obtain an accurate particle segmentation. Due to the sample's aggregate nature, we were able to expand this size range to approximately 0.3 mm for the ilastik model and approximately 0.5 mm for the Dragonfly model. In this project, the ilastik model returned an approximated power-law slope of -2.91 and the Dragonfly model returned a power-law slope of -2.03, meaning that the ilastik model displays a significantly higher frequency of smaller particles than the Dragonfly model. Because of these slope values, we can conclude that despite being a rubble-pile asteroid, Bennu's surface is not void of small particles and we can evaluate Bennu's surface evolution and how the sample may have been altered by agitation during sample collection and Earth return.

## 1 INTRODUCTION

The OSIRIS-REx (Origins, Spectral Interpretation, Resource Identification, and Security-Regolith Explorer) mission collected a roughly 121.6-gram regolith sample from near-Earth asteroid Bennu. The goal of this mission is to investigate the formation and evolution of our solar system (Lauretta et al., 2024). Bennu is a roughly 500-meter, B-type (Jawin et al., 2023), rubble-pile asteroid that was chosen for sample collection due to telescopic observations indicating a carbonaceous composition

33 and the potential of water (Clark et al., 2011). Collecting a sample of Bennu's regolith allowed  
34 for the analysis of a primitive material without the terrestrial contamination that we observe from  
35 meteorites (Lauretta et al., 2024). The entire sample of Bennu's regolith was sorted into over 100  
36 sample IDs, some containing single, large particles and others containing a collection of smaller  
37 particles varying in size.

38 A particle size frequency distribution (PSFD) display how many particles fall within a certain  
39 size range. The longest axis of each particle within a sample can be determined using a variety of  
40 different image processing software. The frequency of the particle size can be determined within  
41 these image processing software or using a coding script. The PSFD of an asteroid can tell us many  
42 different aspects of the asteroid. Firstly, it can provide insights regarding the evolution of the surface  
43 of the asteroid which in turn, can provide insights into the evolution of our solar system. Considering  
44 that Bennu is assumed to be a rubble-pile asteroid, Bennu is made of many independent particles,  
45 all held together by the cohesive forces between particles and the asteroid's weak self-gravitation.  
46 We know that the gravity is weak on the surface of Bennu due to how the Nightingale sample site  
47 responded to sample collection. An analysis of the collection site within Hokioi crater was conducted  
48 before and after sample collection and it was found that there was a significant change in the surface  
49 of Bennu caused by the sampling event (Lauretta et al., 2022), including a change in topography,  
50 surface height, and reflectance by Bennu's subsurface being exposed. From Bennu's PSFD from an  
51 aggregate sample, we can determine the power-law slope for particle sizes smaller than what has  
52 previously been determined. This will allow us to understand how many small particles make up  
53 Bennu relative to the larger particles and how these small particles affect the nature of Bennu.

54 We have determined that asteroid Bennu is a rubble-pile asteroid and therefore can assume that  
55 Bennu should have more small particles than large particles. Burke et al. (2021) shows in figure 1  
56 that the PSFD for the Nightingale collection site has a relatively steep slope, indicating a greater  
57 frequency of smaller particles. Because the Recon C power-law slope was determined using measure-  
58 ments with the highest resolution of the four mission stages, we assume that this power-law slope  
59 most accurately represents the surface of asteroid Bennu. In addition to the findings in Burke et al.  
60 (2021), Dr. Filippo Tusberti and Dr. Maurizio Pajola produced a PSFD with a power-law slope  
61 of  $-2.1 \pm 0.1$  for a particle size range of 1.1 mm to 36.6 mm which is a very similar power-law  
62 slope to the Recon C measurement from Burke et al. (2021). This further supports that the Recon  
63 C power-law slope from ? is an accurate representation of Bennu's regolith, even at smaller particle  
64 diameters than those measured by the Recon C project.

65 While Dr. Filippo Tusberti and Dr. Maurizio Pajola significantly extended the understanding  
66 of power-law slope from a lower limit of approx. 50 mm to a lower limit of 1.1 mm, we do have  
67 samples of Bennu's regolith containing particles smaller than 1.1 mm. We have analyzed sample  
68 OREX-800107-0 which is a 6.4-gram aggregate sample containing roughly 2 million particles with a  
69 size range of less than 0.017 mm to approximately 6 mm. In this paper, we will discuss the process  
70 of segmenting the particles in OREX-800107-0 using machine learning algorithms and determining

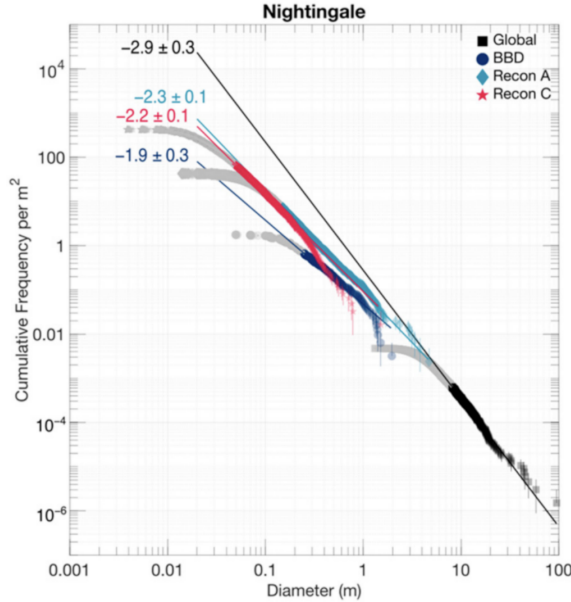


Figure 1: This figure shows the cumulative PSFD of asteroid Bennu calculated at four mission phases. The y-axis represents the cumulative frequency of particles per square meter and the x-axis represents the diameter of the particle in meters. The global measurement was determined using early images of Bennu from DellaGiustina et al. (2019) and the recon C measurement was determined using higher-resolution imaging with a pixel scale of approx. 0.004 meters. The light gray data points correspond to "roll-off" where the accuracy of the measurements is uncertain and would negatively affect the determined power-law slope if they were included in the PSFD. These power-law slopes serve as the expected values for PSFD analysis for asteroid Bennu (Burke et al., 2021).

71 each particle's longest axis in order to produce a PSFD. This power-law slope determination for  
 72 OREX-800107-0 (image of the sample shown in figure 2) can be added to the previous PSFDs for  
 73 asteroid Bennu to analyze if the power-law slope remains constant as particle size decreases.

## 74 2 METHODS

75 Through image processing, it was essential to account for as many particles as possible while not  
 76 compromising the accuracy of the measurements of the particles. While there are many software  
 77 options for image processing, the two main software programs used in this experiment were the ones  
 78 that provided the most promising results for the least amount of manual correction. These two  
 79 programs were *Dragonfly* and *ilastik*. Once the particles were segmented as shown in figure 4, the  
 80 longest axis of each particle was computed in order to compose the PSFD.

81 The main difficulty when analyzing this sample was the limitations of voxel classification due to  
 82 the resolving power of the X-Ray Computed Tomography (XCT) data. The XCT data has a voxel  
 83 size of 0.017 mm. Any particles with a diameter of less than 0.017 mm simply could not be resolved

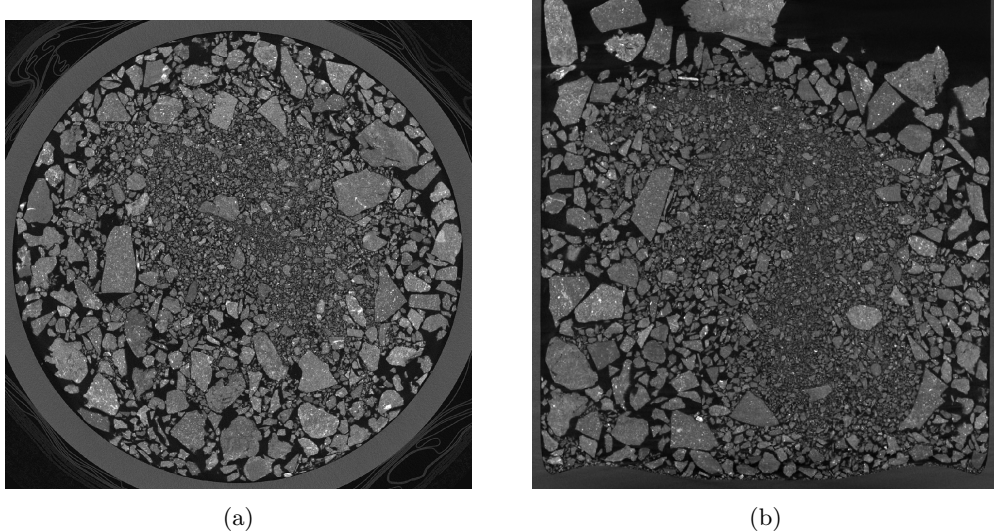


Figure 2: This figure displays two different views of the XCT data of sample OREX-800107-0. Figure 2a shows the sample in the xy-plane at z-slice 800 out of 1719. Figure 2b shows the same sample in the xz-plane at y-slice 700 out of 1383.

as a particle. Any particles that were relatively small were difficult to accurately segment, as shown in figure 3. When viewing the sample as a whole (figure 3a), it seems relatively easy for the human eye to separate the distinct particles, even among the unresolved material. As we get closer to the unresolved material and the voxels become more distinct (figures 3c and 3d), the boundaries between the particles become less obvious, even to the human eye, with it being near impossible to accurately determine which voxels are to be assigned to each particle. Although the human eye is extremely capable of detecting patterns, the machine learning algorithms use the grayscale of the XCT data to classify the voxels. This means that if there is not enough of a difference between the color of the voxels, the algorithm will quickly lose accuracy in those areas. The machine learning algorithms either failed to segment the small particles together— resulting in an inaccurate large particle in the segmentation— or failed to recognize the proper shape of the small particle— resulting in inconsistencies with the accurate shape and size of the particle which can be seen in figure 7.

## 2.1 Experimental Design

This sample of asteroid Bennu was a roughly 6.4-gram aggregate sample, meaning that isolating and marking each individual grain was difficult. The sample has an estimated one to two million particles so we needed to find a method to separate these particles without needing to add manual correction. We started the image processing with the *Dragonfly* software but encountered difficulties with obtaining accurate results and had technological limitations. We particularly focused on using a modified watershed technique (Zheng and Hryciw, 2016) which seemed promising for the large range of shapes and sizes that exist in the sample. We quickly found that as we shrunk the particle mask in order to account for the smaller particles, we lost information about the larger particles. If

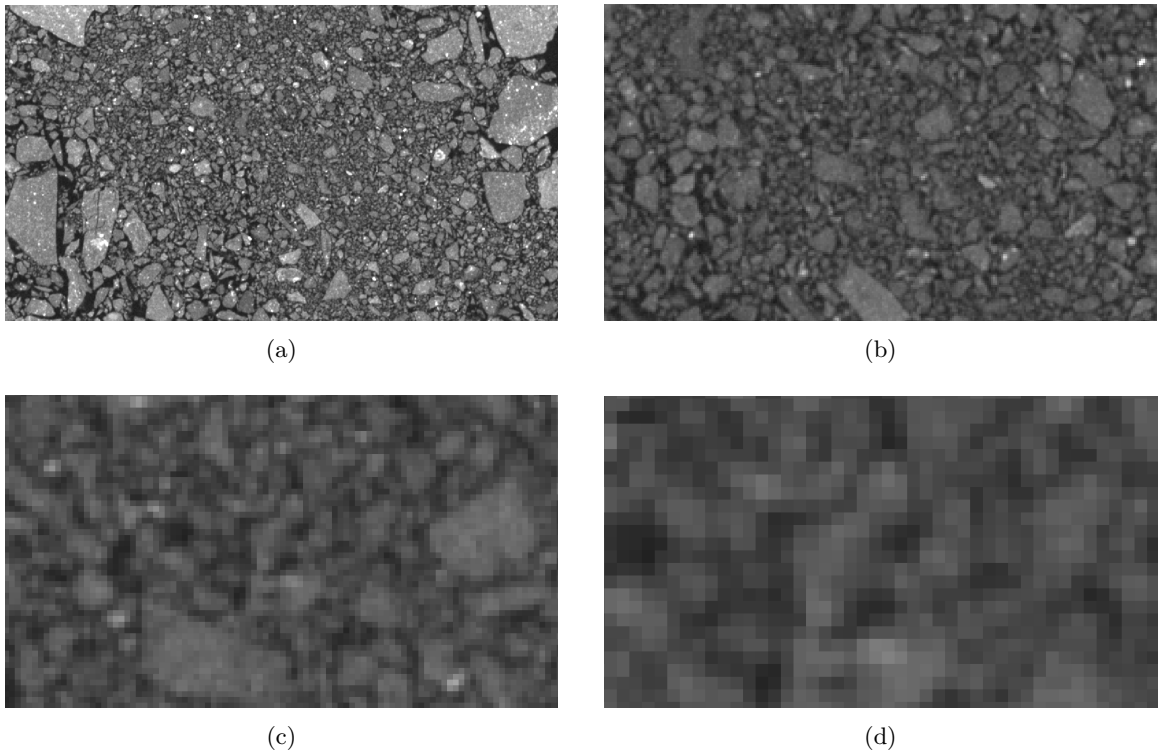


Figure 3: This figure shows the unresolved material at various viewpoints. From figure 3a to figure 3d, the voxels become clearer and the issue with the smallest particles becomes more apparent due to our limitations with the voxel size of the XCT data.

we kept the mask relatively large, the smaller particles were collected together and would therefore be accounted for as larger particles, making it difficult to sort these objects out during the analysis stage. We then used *ilastik* software (Berg et al., 2019) that exclusively used user annotations. For both *ilastik* and *Dragonfly* software programs, the XCT data was input as a stack of TIFF images along the z-axis, and the machine learning algorithms were trained in two dimensions and then applied to the three-dimensional data set. Three classes of materials were hand-labeled in each software: distinct particles, void space (including very small or unresolved particles), and the stainless-steel sample container walls.

### 2.1.1 **ilastik**

We trained a convolutional neural network using a Random Forest machine learning algorithm within the *ilastik* software. *ilastik* uses small user annotations to assign classification labels to individual pixels. From these annotations, the algorithm generates a probability for the classification of every pixel and the user can add more annotations to refine the probabilities and therefore refine the final data segmentation. We trained three small regions varying in size every 100 slices along each axis. We used smaller regions for unresolved material areas and larger regions for vessel areas and areas with a large number of particle-to-particle contacts. Minimal training was done when

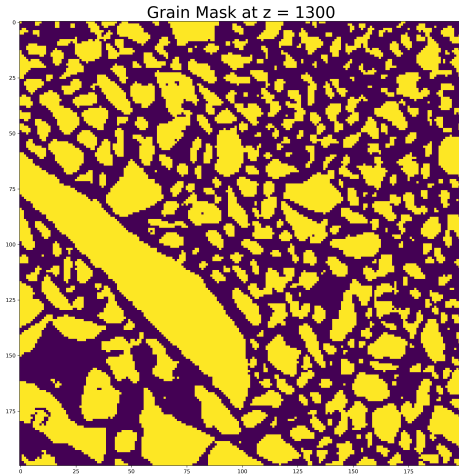


Figure 4: This figure shows the particle mask from ilastik that was used for the longest axis approximation for the particles. This mask is taken from z-slice 1300 out of 1719. Yellow corresponds to particles and purple corresponds to background and unresolved material. This is the mask that is used throughout the Python script to calculate the longest axis of each particle.

possible to avoid over-training and confusing the classifier. While training this model, we focused on minimizing the two anticipated sources of error. The first source of error is the improper classification of unresolved material and the second source of error is the lack of identification of the contacts between particles.

### 2.1.2 Dragonfly

We trained a convolutional neural network for semantic segmentation using the Segmentation Wizard within the Dragonfly software platform. We utilized the built-in two-dimensional U-net convolutional network, which uses extensive data augmentation (e.g., flipping and warping of the training images) to produce a satisfactory result with a small training dataset. Training data (Figure X) initially consisted of 5 small sub-regions (approx. 3–10 mm each in size) where the three classes of materials were hand-labeled. Care was taken to add space voxels along particle-to-particle contacts so as to separate them. In areas with dense concentrations of fine and unresolved particles, we adopted a conservative approach by only labeling particles with distinct, easily recognizable boundaries (typically greater than a few hundred microns in size). As the CNN predictions improved with more training data, the CNN was applied to other slices in the dataset to identify areas where materials were mislabeled. These areas were manually corrected and added to the training dataset for subsequent retraining of the network. This process was continued until a heuristic point of diminishing returns was reached, accomplished via visual inspection of test slices where the model was applied. Model training was terminated when all large, distinct particles were accurately labeled in a few test slices, with particular attention paid to the separation of particles via the labeling of

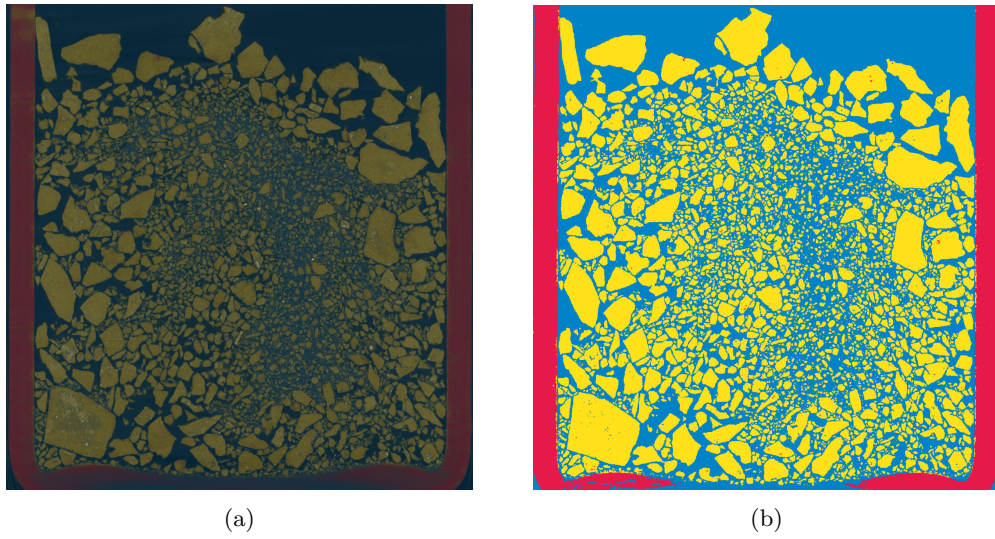


Figure 5: This figure shows the particle segmentation that resulted from the Random Forest machine learning algorithm within the ilastik software. Figure 5a shows the probability of all the classes for a slice of the sample. Yellow voxels are counted as particles. Figure 5b shows the actual segmentation of the particles. Several instances of misclassifications can be seen with these images, particularly along the border of the container, shown in red.

<sup>141</sup> space voxels at their contacts so as to create unconnected voxel islands for each particle.

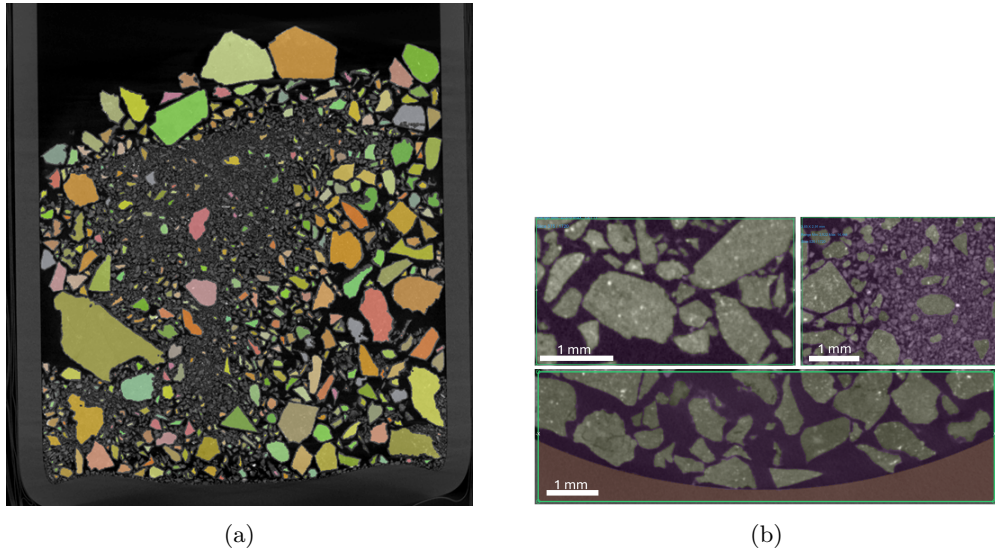


Figure 6: This figure shows the particle segmentation that resulted from the Segmentation Wizard within the Dragonfly software. Figure 6a shows the entire sample’s particle segmentation where each color corresponds to a different particle. Figure 6b shows three regions with the probability of the segmentation for the three different classes, with the top right image showing the segmentation probability for some unresolved material.

142    **2.2 Computational Analysis**

143    Once the sample was the training model was considered to meet our standards of accuracy, the  
144    segmentation was analyzed using Python script. We used *SciPy* (Virtanen et al., 2020) modules  
145    *ndimage* and *spatial* to label every particle in the sample data and determine the longest axis of each  
146    particle in millimeters. We used a slightly different approach depending on which image processing  
147    software the particle segmentation was coming from.

148    **2.2.1 ilastik**

149    For the ilastik segmentation, we imported the three-dimensional particle segmentation as a stack  
150    of TIFF images and determined which voxels belonged to each class. We then used a bounding  
151    box algorithm using the *find\_objects* function which finds and returns the vertices of the box that  
152    bounds each particle in the sample. The longest axis of the particle was approximated by calculating  
153    the longest diagonal of the bounding box. This approximation was made due to the fact that  
154    computing the true longest axis by counting voxels is very computationally expensive but future  
155    work will not depend on the bounding box approximation. Once the longest axis of each particle  
156    was approximated, the PSFD with a normalized cumulative frequency count was plotted using the  
157    *matplotlib* library.

158    **2.2.2 Dragonfly**

159    For the Dragonfly segmentation, the computational analysis was much simpler. Once the machine  
160    learning algorithm had been accurately trained, the maximum Feret diameter—the maximum dis-  
161    tance one could measure across the particle with a ruler—was calculated using tools within the  
162    Dragonfly software. These diameters were exported from Dragonfly as a CSV file and read into the  
163    Python script to plot the PSFD using the *matplotlib* library once again.

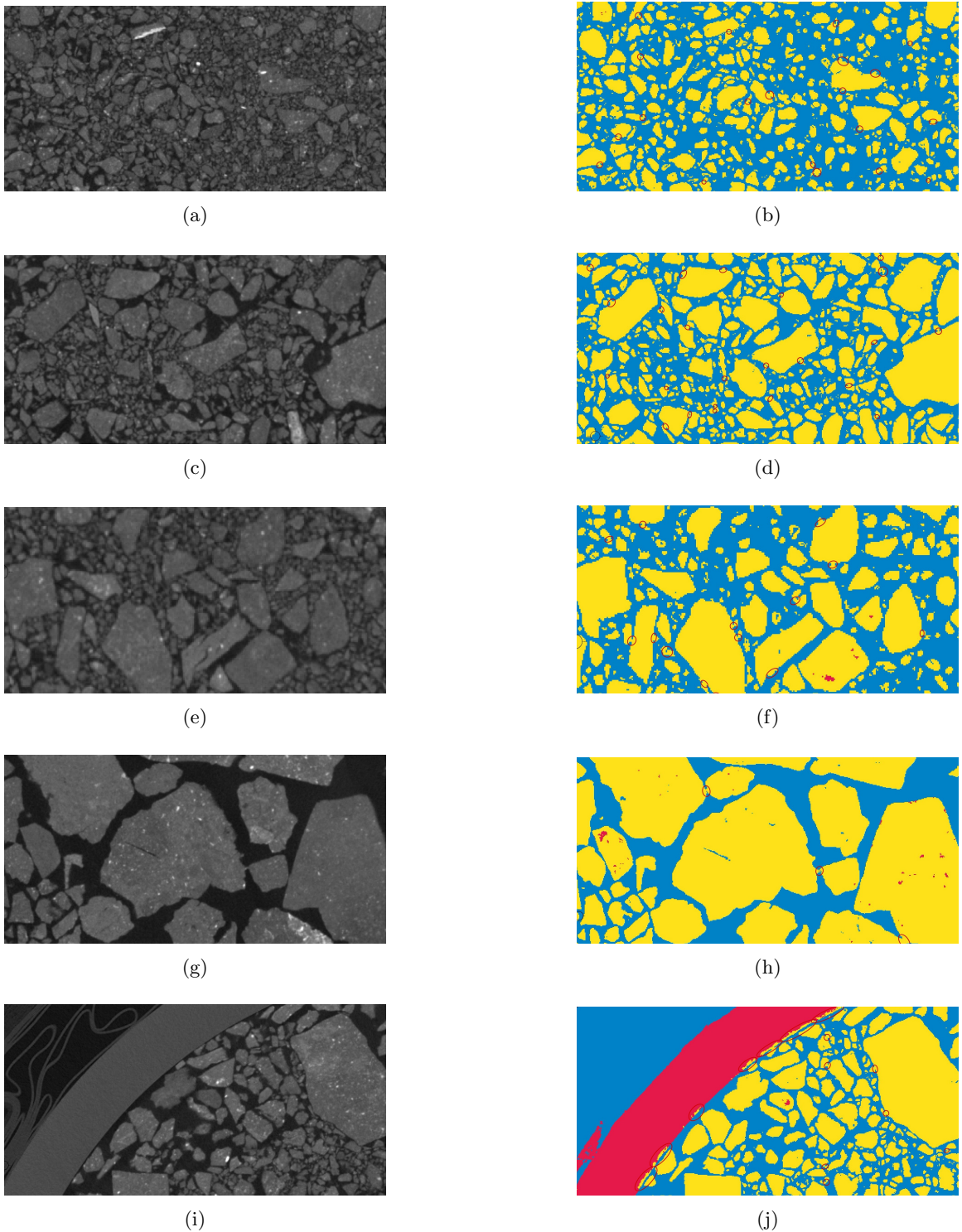


Figure 7: These figures show the XCT data compared to the particle segmentation produced by the machine learning algorithm within the ilastik software. Regions circled in red on the figures in the right column are areas that do not accurately reflect the sample. Note that the ilastik model has trouble with deciphering vessel grayscale from particle grayscale in some regions.

164 **3 RESULTS AND DISCUSSION**

165 **3.1 RESULTS**

166 Due to the drop-off nature of the PSFD, we qualitatively chose a lower and upper cut-off point  
167 for the PSFD power-law slope so that the slope calculation most accurately reflected the linear  
168 portion of the PSFD. Using these qualitative cut-offs, we determined the power-law slope with a  
169 lower limit of 0.2 mm for the ilastik model and 0.5 mm for the Dragonfly model, 0.9 mm and 0.6  
170 mm smaller than the measurement from Dr. Filippo Tusberti and Dr. Maurizio Pajola. The error  
171 measurements were calculated to reflect the error in the cumulative frequency of each bin. We used  
172 a Poisson detection distribution uncertainty used in Burke et al. (2021) although we can also use  
173 the Bootstrap uncertainty outlined in Clauset et al. (2009).

174 **3.1.1 ilastik**

175 From the ilastik model, the PFSD in figure 8a reflects a power-law slope of -2.91 for a particle  
176 size range of 0.3 mm to 3.0 mm which is similar to the global measurement from Burke et al. (2021)  
177 which resulted in a PSFD power-law slope of -2.9 +/- 0.3.

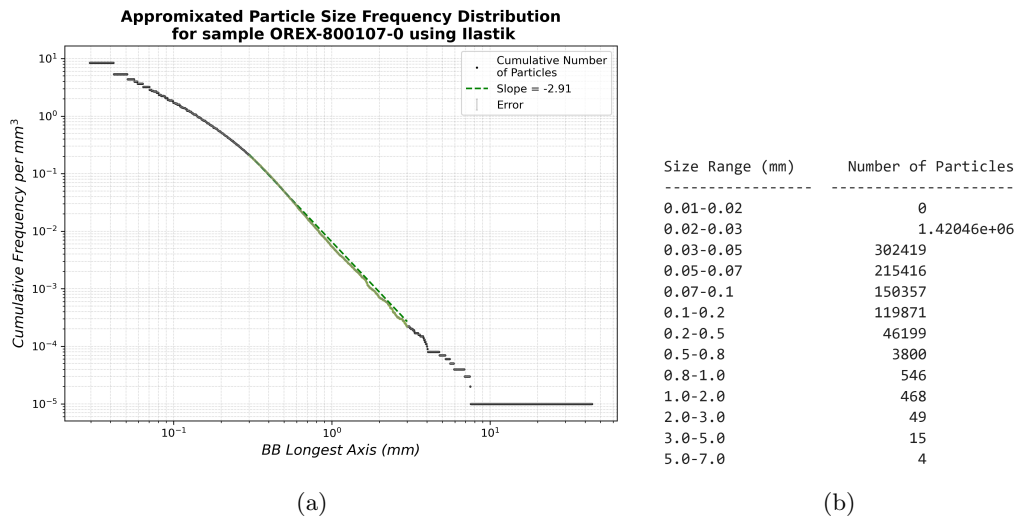
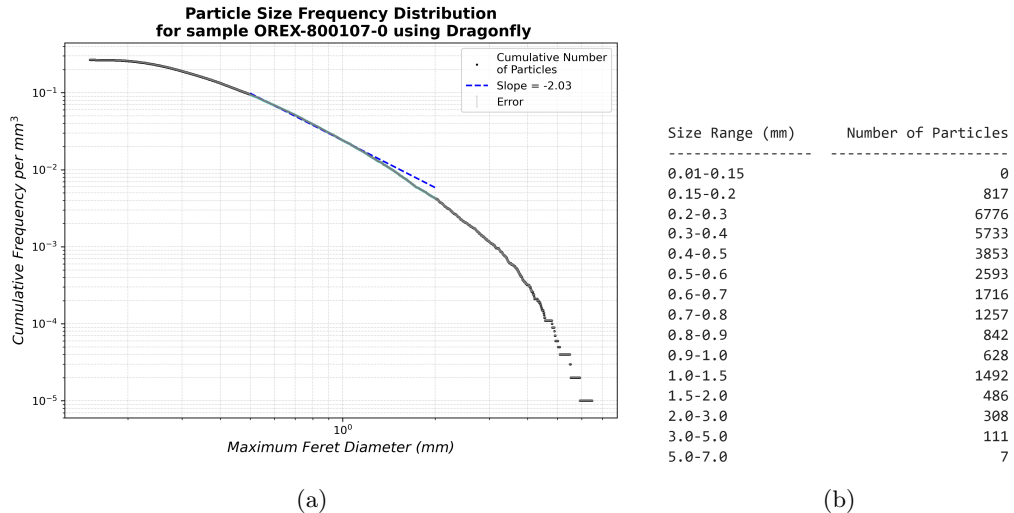


Figure 8: This figure shows the results from the ilastik software. For the PSFD (figure 8a), the x-axis represents the longest axis approximation from the bounding box algorithm in millimeters and the y-axis represents the cumulative frequency per cubic millimeter. The colored region (green) is to highlight the data points that contribute to the calculation of the power-law slope. This PSFD has a power-law slope of -2.91, which is similar to the global measurement from Burke et al. (2021), for a size range of 0.3 mm to 3.0 mm. The table on the right 8b shows the total number of particles in each size range as shown in the left column.

178 **3.1.2 Dragonfly**

179 From the Dragonfly model, the PSFD in figure 9a reflects a power-law slope of -2.03 for a particle  
 180 size range of 0.5 mm to 2.0 mm which is similar to both the BBD (baseball diamond) and the Recon  
 181 C measurement from Burke et al. (2021). The BBD measurement has a power-law slope of  $-1.9 \pm 0.3$   
 182 and the Recon C measurement has a power-law slope of  $-2.2 \pm 0.1$ . This result is also similar  
 183 to the results of Dr. Filippo Tusberti and Dr. Maurizio Pajola who produced a power-law slope of  
 184  $-2.1 \pm 0.1$ , a result very similar to the Recon C measurement.



(a)

(b)

Figure 9: This figure shows the results from the Dragonfly software. For the PSFD (figure 9a, the axes are the same as those for the ilastik model and the colored region (blue) is to highlight the data points that contribute to the calculation of the power-law slope. This PSFD has a power-law slope of -2.03, which is similar to the Recon C measurement from Burke et al. (2021), for a size range of 0.5 mm to 2.0 mm (smaller range than ilastik). The table on the right 9b shows the total number of particles in each size range as shown in the left column.

185 **3.2 DISCUSSION**

186 Results from both machine learning algorithms produced results that aligned with our expectations  
 187 for the power-law slope from Burke et al. (2021) and Dr. Filippo Tusberti and Dr. Maurizio Pajola.  
 188 Although neither result seems unreasonable, the Dragonfly model aligns more with the power-law  
 189 slope that we expect from the above researchers. The Recon C measurement was the highest  
 190 resolution survey conducted on the Nightingale sample site (Burke et al., 2021) so we should expect  
 191 that the PSFD for the returned samples reflect this power-law slope. If the power-law slope does  
 192 not reflect the Recon C measurement, then it is essential to ask why it would vary from what the  
 193 surveys told us as the spacecraft was orbiting Bennu. It is possible that the sample was somehow  
 194 altered either during sample collection or earth return but the results from Dr. Filippo Tusberti  
 195 and Dr. Maurizio Pajola seem to reflect that the sample was kept remarkably safe (because the  
 196 power-law slopes were so similar). The power-law slopes could also vary due to the aggregate nature

197 of the sample and the possibility that there was a small amount of material from the subsurface that  
198 contained much smaller particles than what was able to be viewed from the spacecraft.

199 These slopes from the PSFDs shown in figure 8a and figure 9a mean that asteroid Bennu is not  
200 void of small particles, despite being a rubble-pile asteroid. Having an accurate value for the power-  
201 law slope of the PSFD for asteroid Bennu can allow us to make claims about the evolution of the  
202 surface of Bennu. Because we have determined power-law slopes for the asteroid itself and for the  
203 regolith samples that have been returned to earth, we can compare these slopes to infer if the sample  
204 remained as pure as we had hoped.

## 205 4 CONCLUSION

206 We determined two power-law slopes— -2.91 for the ilastik model and -2.03 for the Dragonfly  
207 model— for a size range of 0.3 mm to 3.0 mm and 0.5 mm to 2.0 mm respectively. These results  
208 have extended the previous lower limit for the PSFD power-law slope of 1.1 mm. Both the ilastik  
209 and Dragonfly machine learning models provided sensical results given the previous power-law slopes  
210 determined in Burke et al. (2021) although the power-law slope resulting from Dragonfly was more  
211 aligned with our expected value from the Recon C measurement.

212 The most important next step will be to improve the accuracy of the results shown above. As  
213 shown in figure 7, there are many regions where the machine learning algorithm needs to be manually  
214 corrected so that the classification prediction more accurately represents the sample data. We can  
215 analyze the accuracy of the segmentation by choosing a random slice and comparing the segmentation  
216 to the XCT data, similar to the images shown in figure 7. Once the CNN seems to accurately predict  
217 the shape and size of the particle, we can be more confident in our results shown in the PSFDs. From  
218 this power-law slope determination, we can also analyze the shape properties of the particle found in  
219 OREX-800107-0. Mainly, we can determine the sphericity and roundness of the particles from their  
220 dimensions which can lead to classifications of angular and hummocky particles (Gowman et al.,  
221 2023). Angular particles are those that are relatively uniform and have clear, sharp boundaries.  
222 Hummocky particles are those that are non-uniform and tend to be made up of many different  
223 grains compacted together. Within the PSFD measurements, there may be a difference between  
224 these two types of particles and therefore we may be able to produce a separate PSFD for each type.  
225 Comparing this to the already determined PSFD power-law slopes for Bennu can give us insight into  
226 whether or not we are biased toward one type of particle in our measurements. Also, the power-law  
227 slopes of the PSFDs for Bennu could reveal some information about the relative strength of the  
228 asteroid Bennu. We know Bennu is a rubble-pile asteroid (Pajola et al., 2024) but we also know  
229 that Bennu is *not* void of small particles so it is clear that Bennu has enough self-gravitation that  
230 not all small particles fly off of its surface. Although Lauretta et al. (2022) explains that during  
231 the TAGSAM event, the surface of Bennu was significantly disturbed, with the subsurface being  
232 exposed post-collection. Lastly, the findings of asteroid Bennu can be compared to other rubble-pile  
233 asteroids such as Ryugu in order to improve our understanding of asteroids as a whole.

234 **Acknowledgments**

235 This work was funded by the NASA Arizona Space Grant Consortium in works with the NASA  
236 OSIRIS-REx mission as a part of the Spatial, Physical, and Thermal Analysis team. We thank  
237 Scott Eckley at the NASA Goddard Space Flight Center for collecting the XCT data (Eckley, Scott,  
238 2025) and we thank all those part of the OSIRIS-REx sample analysis team who have contributed  
239 their ideas to this work.

240 Dragonfly 2024.1 [Computer software]. Comet Technologies Canada Inc., Montreal, Canada; soft-  
241 ware available at <https://dragonfly.comet.tech/>

242 **References**

- 243 Berg, S., Kutra, D., Kroeger, T., Straehle, C. N., Kausler, B. X., Haubold, C., Schiegg, M., Ales,  
244 J., Beier, T., Rudy, M., Eren, K., Cervantes, J. I., Xu, B., Beuttenmueller, F., Wolny, A., Zhang,  
245 C., Koethe, U., Hamprecht, F. A., and Kreshuk, A. (2019). ilastik: interactive machine learning  
246 for (bio)image analysis. *Nature Methods*.
- 247 Burke, K. N., DellaGiustina, D. N., Bennett, C. A., Walsh, K. J., Pajola, M., Bierhaus, E. B., Nolan,  
248 M. C., Boynton, W. V., Brodbeck, J. I., Connolly Jr., H. C., Deshpriya, J. D. P., Dworkin, J. P.,  
249 Elder, C. M., Golish, D. R., Hoover, R. H., Jawin, E. R., McCoy, T. J., Michel, P., Molaro, J. L.,  
250 Nolau, J. O., Padilla, J., Rizk, B., Robbins, S. J., Sahr, E. M., Smith, P. H., Stewart, S. J.,  
251 Susorney, H. C. M., Enos, H. L., and Lauretta, D. S. (2021). Particle size-frequency distributions  
252 of the osiris-rex candidate sample sites on asteroid (101955) bennu. *Remote sensing*, 13:15.
- 253 Clark, B. E., Binzel, R. P., Howell, E. S., Cloutis, E. A., Ockert-Bell, M., Christensen, P., Barucci,  
254 M. A., DeMeo, F., Lauretta, D. S., Connolly Jr., H., Soderberg, A., Hergenrother, C., Lim, L.,  
255 Emery, J., and Mueller, M. (2011). Asteroid (101955) 1999 rq36: Spectroscopy from 0.4 to 2.4m  
256 and meteorite analogs. *Icarus*, 216(2):462–475.
- 257 Clauset, A., Shalizi, C. R., and Newman, M. E. J. (2009). Power-law distributions in empirical data.  
258 *SIAM Review*, 51(4):661–703.
- 259 DellaGiustina, D. N., Emery, J. P., Golish, D. R., Rozitis, B., Bennett, C. A., Burke, K. N., Ballouz,  
260 R.-L., Becker, K. J., Christensen, P. R., Drouet d'Aubigny, C. Y., Hamilton, V. E., Reuter, D. C.,  
261 Rizk, B., Simon, A. A., Asphaug, E., Bandfield, J. L., Barnouin, O. S., Barucci, M. A., Bierhaus,  
262 E. B., Binzel, R. P., Bottke, W. F., Bowles, N. E., Campins, H., Clark, B. C., Clark, B. E.,  
263 Connolly, H. C. J., Daly, M. G., de Leon, J., Delbo', M., Deshpriya, J. D. P., Elder, C. M.,  
264 Fornasier, S., Hergenrother, C. W., Howell, E. S., Jawin, E. R., Kaplan, H. H., Karefa, T. R.,  
265 Le Corre, L., Li, J.-Y., Licandro, J., Lim, L. F., Michel, P., Molaro, J., Nolan, M. C., Pajola, M.,  
266 Popescu, M., Rizos Garcia, J. L., Ryan, A., Schwartz, S. R., Shultz, N., Siegler, M. A., Smith,  
267 P. H., Tatsumi, E., Thomas, C. A., Walsh, K. J., Wolner, C. W. V., Zou, X.-D., Lauretta, D. S.,  
268 and Team, T. O.-R. (2019). Properties of rubble-pile asteroid (101955) bennu from osiris-rex  
269 imaging and thermal analysis. *Nature Astronomy*, 3:341–351.

- 270 Eckley, Scott (2025). X-ray ct data for bennu aggregate sample orex-800107-0.
- 271 Gowman, G., Cotto-Figueroa, D., Ryan, A., Garvie, L. A. J., Hoover, C. G., and Asphaug, E.  
272 (2023). Roughness and angularity of fragments from meteorite disruption experiments. *The  
273 Planetary Science Journal*, 187.
- 274 Jawin, E. R., Ballouz, R.-L., Ryan, A. J., Kaplan, H. H., McCoy, T. J., Al Asad, M. M., Molaro, J. L.,  
275 Rozitis, B., and Keller, L. P. (2023). Boulder diversity in the nightingale region of asteroid (101955)  
276 bennu and predictions for physical properties of the osiris-rex sample. *Journal of Geophysical  
277 Research: Planets*, 128:22.
- 278 Lauretta, D. S., Adam, C. D., Allen, A. J., Ballouz, R.-L., Barnouin, O. S., Becker, K. J., Becker,  
279 T., Bennett, C. A., Bierhaus, E. B., Bos, B. J., Burns, R. D., Campins, H., Cho, Y., Christen-  
280 tensen, P. R., Church, E. C. A., Clark, B. E., Connolly, H. C., Daly, M. G., DellaGiustina, D. N.,  
281 Drouet d'Aubigny, C. Y., Emery, J. P., Enos, H. L., Freund Kasper, S., Garvin, J. B., Getz-  
282 danner, K., Golish, D. R., Hamilton, V. E., Hergenrother, C. W., Kaplan, H. H., Keller, L. P.,  
283 Lessac-Chenen, E. J., Liounis, A. J., Ma, H., McCarthy, L. K., Miller, B. D., Moreau, M. C.,  
284 Morota, T., Nelson, D. S., Nolau, J. O., Olds, R., Pajola, M., Pelgrift, J. Y., Polit, A. T., Ravine,  
285 M. A., Reuter, D. C., Rizk, B., Rozitis, B., Ryan, A. J., Sahr, E. M., Sakatani, N., Seabrook,  
286 J. A., Selznick, S. H., Skeen, M. A., Simon, A. A., Sugita, S., Walsh, K. J., Westermann, M. M.,  
287 Wolner, C. W. V., and Yumoto, K. (2022). Spacecraft sample collection and subsurface excavation  
288 of asteroid (101955) bennu. *Science*, 377(6603):285–291.
- 289 Lauretta, D. S., Connolly, H. C. J., Aebersold, J. E., Alexander, C. M. O., Ballouz, R.-L., Barnes,  
290 J. J., Bates, H. C., Bennett, C. A., Blanche, L., Blumenfeld, E. H., Clemett, S. J., Cody, G. D.,  
291 DellaGiustina, D. N., Dworkin, J. P., Eckley, S. A., Foustoukos, D. I., Franchi, I. A., Glavin,  
292 D. P., Greenwood, R. C., Haenecour, P., Hamilton, V. E., Hill, D. H., Hiroi, T., Ishimaru, K.,  
293 Jourdan, F., Kaplan, H. H., Keller, L. P., King, A. J., Koefoed, P., Kontogiannis, M. K., Le, L.,  
294 Macke, R. J., McCoy, T. J., Milliken, R. E., Najorka, J., Nguyen, A. N., Pajola, M., Polit, A. T.,  
295 Righter, K., Roper, H. L., Russell, S. S., Ryan, A. J., Sandford, S. A., Schofield, P. F., Schultz,  
296 C. D., Seifert, L. B., Tachibana, S., Thomas-Keprrta, K. L., Thompson, M. S., Tu, V., Tusberti,  
297 F., Wang, K., Zega, T. J., Wolner, C. W. V., and Team, O.-R. S. A. (2024). Asteroid (101955)  
298 bennu in the laboratory: Properties of the sample collected by osiris-rex. *Meteoritics Planetary  
299 Science*, pages 1–34.
- 300 Pajola, M., Tusberti, F., Lucchetti, A., Barnouin, O., Cambioni, S., Ernst, C. M., Dotto, E., Daly,  
301 R. T., Poggiali, G., Hirabayashi, M., Nakano, R., Mazzotta Epifani, E., Chabot, N. L., Della Corte,  
302 V., Rivkin, A., Agrusa, H., Zhang, Y., Penasa, L., Ballouz, R.-L., Ivanovski, S., Murdoch, N.,  
303 Rossi, A., Robin, C., Ieva, S., Vincent, J. B., Ferrari, F., Raducan, S. D., Campo-Bagatin,  
304 A., Parro, L., Benavidez, P., Tancredi, G., Karatekin, , Trigo-Rodriguez, J. M., Sunshine, J.,  
305 Farnham, T., Asphaug, E., Deshapriya, J. D. P., Hasselmann, P. H. A., Beccarelli, J., Schwartz,  
306 S. R., Abell, P., Michel, P., Cheng, A., Brucato, J. R., Zinzi, A., Amoroso, M., Pirrotta, S.,  
307 Impresario, G., Bertini, I., Capannolo, A., Caporali, S., Ceresoli, M., Cremonese, G., Dall'Ora,

- 308 M., Gai, I., Gomez Casajus, L., Gramigna, E., Lasagni Manghi, R., Lavagna, M., Lombardo,  
309 M., Modenini, D., Palumbo, P., Perna, D., Tortora, P., Zannoni, M., and Zanotti, G. (2024).  
310 Evidence for multi-fragmentation and mass shedding of boulders on rubble-pile binary asteroid  
311 system (65803) didymos. *Nature Communications*, 15:13.
- 312 Virtanen, P., Gommers, R., Oliphant, T. E., Haberland, M., Reddy, T., Cournapeau, D., Burovski,  
313 E., Peterson, P., Weckesser, W., Bright, J., van der Walt, S. J., Brett, M., Wilson, J., Millman,  
314 K. J., Mayorov, N., Nelson, A. R. J., Jones, E., Kern, R., Larson, E., Carey, C. J., Polat, İ.,  
315 Feng, Y., Moore, E. W., VanderPlas, J., Laxalde, D., Perktold, J., Cimrman, R., Henriksen, I.,  
316 Quintero, E. A., Harris, C. R., Archibald, A. M., Ribeiro, A. H., Pedregosa, F., van Mulbregt, P.,  
317 and SciPy 1.0 Contributors (2020). SciPy 1.0: Fundamental Algorithms for Scientific Computing  
318 in Python. *Nature Methods*, 17:261–272.
- 319 Zheng, J. and Hryciw, R. D. (2016). Segmentation of contacting soil particles in images by modified  
320 watershed analysis. *Computers and Geotechnics*, 73:142–152.